Realization of high T_i plasmas and confinement characteristics of ITB plasmas in the LHD deuterium experiments

H. Takahashi[1,2], K. Nagaoka[1,3], K. Mukai[1,2], M. Yokoyama[1,2], S. Murakami[4], S. Ohdachi[1,2], T. Bando[5], Y. Narushima[1,2], H. Nakano[1,2], M. Osakabe[1,2], K. Ida[1,2], M. Yoshinuma[1,2], R. Seki[1,2], H. Yamaguchi[1], K. Tanaka[1], M. Nakata[1,2], F. Warmer[6], T. Oishi[1,2], M. Goto[1,2], S. Morita[1,2], T.I. Tsujimura[1], S. Kubo[1,7], T. Kobayashi[1,2], I. Yamada[1], C. Suzuki[1], M. Emoto[1], T. Ido[1,7], A. Shimizu[1], T. Tokuzawa[1], K. Nagasaki[8], T. Morisaki[1,2], Y. Takeiri[1,2] and the LHD Experiment Group[1]

[1]National Institute for Fusion Science, National Institutes of Natural Sciences, Gifu, Japan
[2]SOKENDAI (The Graduate University for Advanced Studies), Gifu, Japan
[3]Department of Physics, Nagoya University, Nagoya, Japan
[4]Department of Nuclear Engineering, Kyoto University, Kyoto, Japan
[5]Fusion Energy Research and Development Directorate, National Institutes for Quantum and Radiological Science and Technology, Ibaraki, Japan
[6]Max Planck Institute for Plasma Physics, Greifswald, Germany
[7]Department of Energy Engineering and Science, Nagoya University, Nagoya, Japan
[8]Institute of Advanced Energy, Kyoto University, Kyoto, Japan

E-mail contact of main author: takahashi.hiromi@lhd.nifs.ac.jp

Abstract. The deuterium (D) operation was initiated in the LHD in 2017. In the first campaign of the D experiments, we successfully extended the high temperature regime in the LHD. The new record of the ion temperature (T_i) of 10 keV associated with the ion internal transport barrier (ITB) was achieved due to several operational optimization. The thermal confinement characteristics of ITB plasmas were compared between hydrogen and D discharges. The effective ion thermal diffusivity of the ion-ITB plasmas was found to be smaller in the D discharges than that in the H discharges. The profiles of the T_i, the electron density, and the impurity of the high T_i plasmas strongly depended on the magnetic configuration and these profiles tended to peaked in the inward-shifted configuration. It was also found that the electron thermal confinement of the electron-ITB plasmas was clearly improved in the deuterium case. The GKV simulation showed the linear growth rate of TEM/ITG reduced in the plasmas with D both for the ion ITB and the electron ITB plasmas and qualitatively agreed with the tendency of the change in the thermal diffusivity obtained from the power balance analysis.

1. Introduction

Clarifying the mechanism of the isotope effect on the confinement characteristics is one of the most important issues in the nuclear fusion research area for realizing the controlled fusion reactor. The increased plasma performance by the isotope effect has been a long-standing mystery, and both experimental [1-6] and theoretical [7-15] approaches have been conducted in several devices in order to deepen the understanding of the isotope effect on the plasma confinement.

Confinement improvement is also necessary for realization of high-temperature plasmas, and is one of the most important issues in toroidal devices. Since the first observation of H mode [16], various types of improved confinement modes have been observed in tokamaks and helical/stellarator devices. Of these improved confinement modes, an internal-transport

barrier (ITB) is characterized by a steep gradient formation in temperature profiles and a decrease in thermal diffusivity in a plasma core region [17-19].

In the Large Helical Device (LHD), high-T_i accompanied with an ion-ITB (i-ITB) has been achieved in NBI-sustained plasmas [20-24]. The i-ITB observed in the LHD is characterized by centre-peaked T_i profile in contrast with a so-called box-type ITB in tokamaks [17, 25]. The formation of weak negative E_r in the core and the strong positive E_r in the peripheral region were also found [23]. Electron-ITB (e-ITB) relating to the production of high T_e plasmas has been realized in the LHD by strongly centre-focused ECRH beams [26-29]. The radial electric field E_r was measured by charge exchange recombination spectroscopy (CXRS) [30] and/or the heavy ion beam probe (HIBP) [31]. The formation of the strong positive E_r was observed in the core region [26], which well agreed with the prediction of the neoclassical transport theory. An e-ITB has been observed in other helical devices as summarized in Ref. [32], and interest has renewed since the beginning of the operation of the Wendelstein 7-X, with Core Electron Root Plasmas [33].

We initiated the deuterium (D) experiment in March 2017 in order to seek higher performance plasmas and to study the mechanism of the increased performance by isotope effect [34, 35]. The present paper shows the achievement of the high T_i plasmas with D and the comparison results of the confinement characteristics of the ITB plasmas between hydrogen (H) and D obtained in the first campaign of the D experiments in the LHD, and is organized as follows. In section 2, the experimental setup is described. Section 3 treats the extension of the operational regime in high T_i plasmas with several operational optimizations. Section 4 focuses on the isotope effect of the confinement characteristics of the i-ITB plasmas. The comparison of the ion thermal confinement between the i-ITB plasmas with D (W/ D) and without D (W/O D), the configuration dependence of the achieved T_i, and the behaviour of the impurity are described. In section 5, the characteristics of the e-ITB formation and the isotope effect on the electron thermal confinement are discussed. The summary is in section 6.

2. Experimental Setup

The LHD is the largest heliotron device with a major radius R = 3.9 m, a minor radius a = 0.6 m, a pole number of 2 and a toroidal period of 10 [36-40]. The heliotron configurations are produced by a set of helical winding coils and three sets of poloidal field coils, which are all superconducting magnets. The maximum magnetic field on the axis is ~2.9 T. In the LHD, three negative-ion-based NBIs produce neutral beams with the beam energy of 180 keV and total port-through power of 16 MW for H beam and 8 MW for D beam [41]. The negative-NBIs are tangentially injected into LHD plasmas. The positive-ion-based NBIs were perpendicularly injected for ion heating [42] with low energy of 40 keV for H and 60 keV/80 keV for D at maximum. The total-port through power of the perpendicular-NBIs reaches 12 MW for H beam and 20 MW for D beam. Thus the highest NBI power in total is produced by the combination of the tangential NBIs with H and the perpendicular NBIs with D. A high power ECRH system has been operated for preionization and plasma heating [29, 43, 44]. In the present state, three 77 GHz gyrotrons and two 154 GHz gyrotrons are operational for plasma experiments. All of these gyrotrons can generate more than 1 MW power. The heating capability on the LHD has been upgraded year by year. The simultaneous injection power of the NBI and the ECRH reached 31 MW and 5.4 MW, respectively.

3. Operation Optimization for Realizing High T_i plasmas

3.1. Wall Conditioning Using ECRH

Intensive wall conditioning using high power ECRH and/or ICRH with helium gas puffing has been conducted to produce a preferable condition for realizing high T_i plasmas in the LHD [45, 46]. Although the wall conditioning effect on reducing the wall recycling was found to depend on the total input RF energy, and not to depend on whether the RF source was ECRH or ICRH [46], the dependence of RF power on the wall conditioning efficiency has not been clarified. The gyrotrons equipped on the LHD can produce the output power of 1 MW each for several seconds and several hundred kW each for more than 10 seconds. We compared the wall conditioning efficiency using different RF power/pulse duration of 4 MW/2 s (8 MJ/shot) and 1 MW/40 s (40 MJ/shot). Figure 1 shows the dependence of the Dα emission intensity $I_{D\alpha}$ in the wall conditioning discharge on (a) the number of the ECRH discharge conditioning (ECDC) shots and (b) the accumulated input ECRH energy ΣW_{ECRH}. The squares and circles represent the data for 4 MW/2 s and 1 MW/40 s, respectively. The ECRH plasmas for the wall conditioning were produced using 77 and 154 GHz gyrotrons in the presence of the magnetic field B_t of ~2.8 T. Helium was used as the working gas and the line-averaged-electron density n_{e_fir} was maintained around $1x10^{19}$ m^{-3} during each discharge. The numbers of the wall conditioning discharges exceeded 30 for both cases. As can be seen from these figures, the reduction of $I_{D\alpha}$ per conditioning discharge was significant for 1 MW/40 s. Also it was found that the reduction of the $I_{D\alpha}$ scales with the accumulated energy of the injected RF. This means that the effect of the RF wall conditioning does not depend on the RF power but the accumulated RF energy in the present experimental condition. The contents of ions in the ECDC plasmas changed through the series of ECDC operation. The ion ratios of the ECDC plasma (n_H:n_D:n_{He}) were (0.07:0.51:0.42) for the ΣW_{ECRH} of 7.2 MJ, (0.03:0.19:0.78) for 250 MJ, and (0.04:0.09:0.87) for 510 MJ.

Figure 2 shows the time evolution of (a) the port-through-NBI power P_{NBI}, (b) n_{e_fir}, (c) $I_{D\alpha}$, (d) the central ion temperature T_{i0}, and the radial profiles of (e) the electron density n_e, and (f) T_i for three plasmas produced in the different wall condition. Those plasmas were produced without wall conditioning, after the wall conditioning of 35 shots with 4 MW/2 s, and after the wall conditioning of 32 shots with 1 MW/40 s. The variable r_{eff}/a_{99} in the horizontal axis of the Fig. 2 (e) and (f) is the effective minor radius normalized by the averaged minor radius where 99% of the electron stored energy is confined. The plasmas were sustained using high

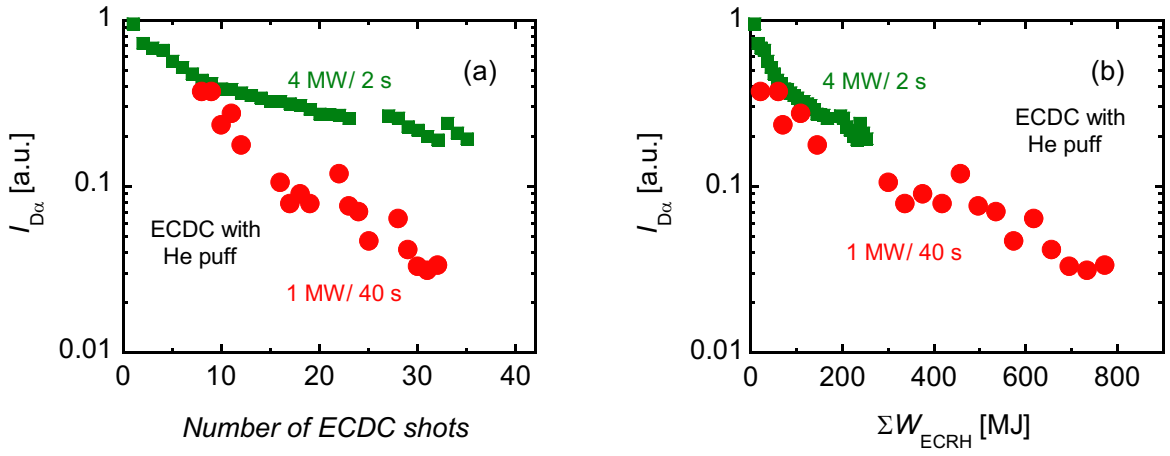

FIG. 1. The dependence of $I_{D\alpha}$ in the wall conditioning discharge on (a) the number of the ECDC shots and (b) the accumulated input ECRH energy.

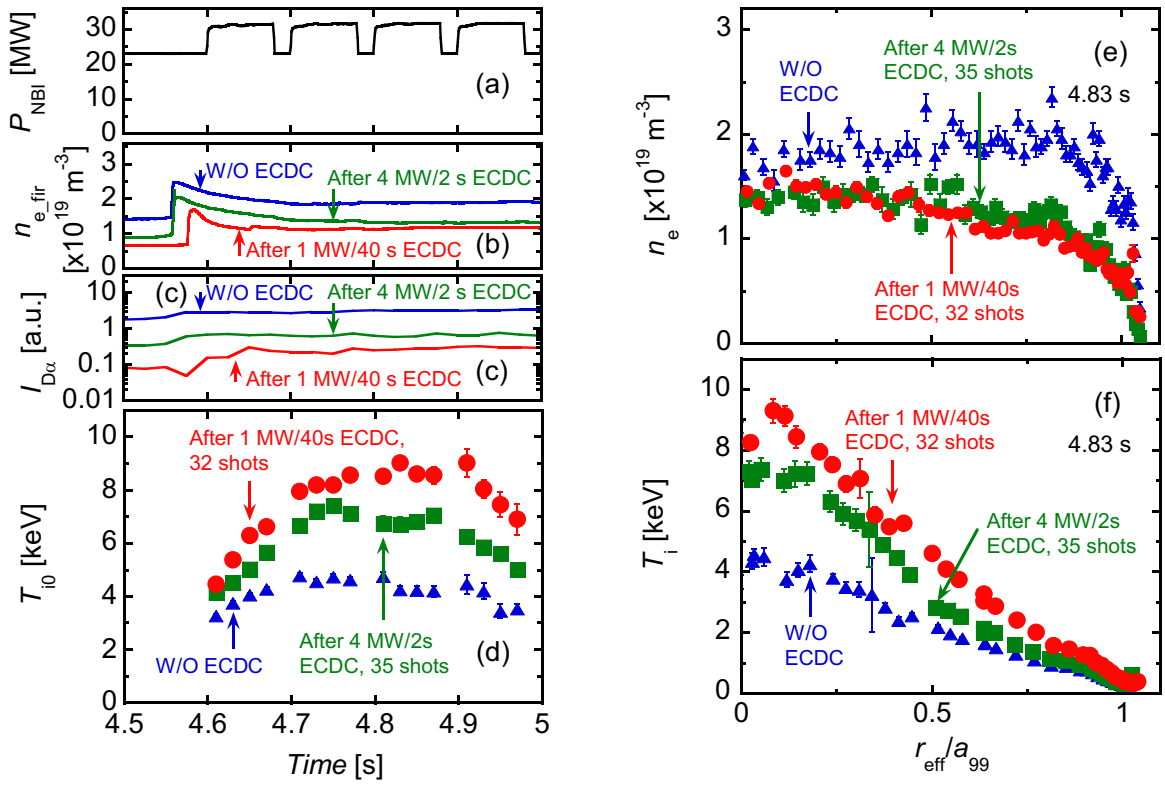

FIG. 2. The time evolution of (a) P_{NBI}, (b) n_{e_fir}, (c) $I_{D\alpha}$, (d) T_{i0}, and the radial profiles of (e) n_e, and (f) T_i for three plasmas produced in the different wall condition. Those plasmas were produced without wall conditioning, after the wall conditioning of 35 shots with 4 MW/2 s, and after the wall conditioning of 32 shots with 1 MW/40 s.

power NBI under the magnetic configuration of R_{ax} = 3.6 m and B_t = 2.85 T with the toroidal magnetic field direction of counter clockwise (CCW), where R_{ax} is the magnetic axis position in vacuum. In order to inject the highest heating power possible, the tangential and perpendicular NBIs were operated using H and D beams, respectively. After the ECDCs, the Dα intensity was clearly reduced during the discharges and higher T_i was obtained compared with no ECDC case. The n_e profile was modified to the peaked shape from the hollow shape due to the application of the ECDC. Also, the lower $I_{D\alpha}$, the higher T_i, and more-peaked n_e profile were realized in the discharge after the 32-shots of 1 MW/40 s ECDC compared with the discharge after the 35-shots of 4 MW/2 s ECDC. This was due to the lower-recycling condition realized by higher energy input of ECDC, as shown in Fig. 1 (b).

3.2. Configuration Dependence on the High T_i Plasma Performance

The magnetic configuration is also the control knob of the plasma performance optimization because the heating profile, the plasma volume, the heat/particle transport, the MHD activities, and the other confinement characteristics were widely changed depending on the magnetic configuration in the LHD [47-53]. Figure 3 shows the radial profiles of (a) n_e, (b) T_e, and (c) T_i sustained using D gas puff and P_{NBI} ~20 MW with all D beams. The circles are the data for the magnetic configuration of R_{ax} = 3.6 m/ B_t = 2.85 T (CCW) and the squares are the data for the inward-shifted configuration of R_{ax} = 3.55 m/ B_t = 2.89 T (CCW). No wall conditioning was conducted in advance of these discharges. Although the T_e profile was similar between these two configurations, higher T_i with the steeper gradient in the plasma core was obtained for the inward-shifted configuration with higher n_e. The n_e profile in R_{ax} =

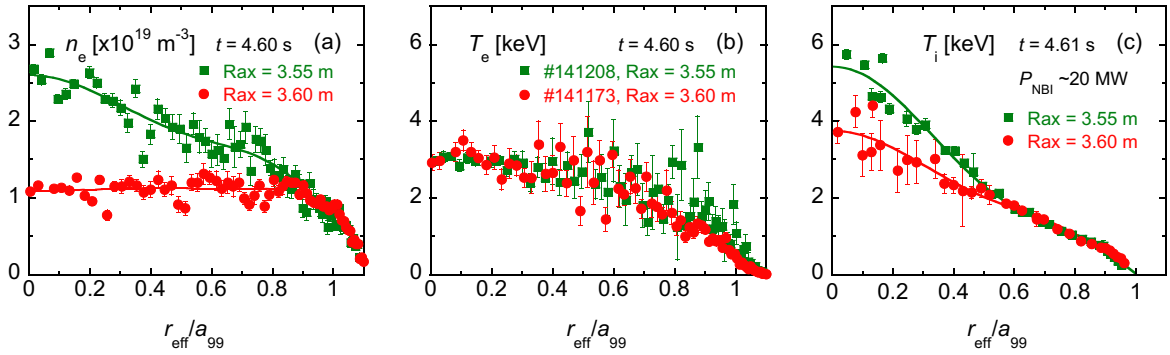

FIG. 3. The radial profiles of (a) n_e, (b) T_e, and (c) T_i in the D plasmas for the magnetic configuration of R_{ax} = 3.6 m (circles) and for the inward-shifted configuration of R_{ax} = 3.55 m (squares).

3.6 m was hollow shape like that W/O ECDC shown in Fig. 2 (e). On the other hand, the n_e profile was found to be peaked for the inward-shifted configuration even though the wall conditioning was not applied. The lower T_e/T_i and the peaked n_e shape contribute to reduce the linear growth rate of ITG/TEM. A more detailed configuration dependence of high-T_i plasma performance is shown in section 4.3.

3.3. Optimization of the Impurity Quantity

Turbulence transport theories predict that a certain amount of impurity contributes to stabilizing an ITG mode [54-56] due to the increase in the effective nuclear charge. Actually, high T_i plasmas have been obtained using impurity pellet injection [57, 58]. In the LHD, the quantity of the injected impurity can be actively controlled by changing the size of the impurity pellet [57, 58]. The optimum carbon density for minimizing the ion thermal diffusivity was found in the previous research in the LHD [58]. Here, the result of the impurity quantity optimization aiming for realization of higher T_i plasmas is shown. Figure 4 shows the dependence of T_{i0} on the number of the carbon atoms injected using the impurity pellet injector. The magnetic configuration was fixed at R_{ax} = 3.6 m and B_t = 2.85 T (CCW). The data were obtained shot by shot using carbon pellets of different sizes. The optimum quantity of injected carbon for obtaining the higher-T_i plasma was found at around 0.7x10^{20} both for the plasmas W/ D and W/O D through the pellet-size scan experiments.

3.4. Achievement of the Highest T_i of the LHD through the Optimizations

In the deuterium phase, we achieved the highest T_i ever obtained in the LHD experiments due to the several operational optimizations with the increased NBI power as mentioned in the sections above. Figure 5 shows the time evolution of (a) P_{NBI}, (b) n_{e_fir}, (c) the normalized magnetic fluctuation b_θ/B_t, (d) the neutron emission rate S_n, (e) the plasma stored energy W_{p_dia}, (f) T_{i0}, and (g) the radial profiles of T_i, T_e, and n_e of the highest-T_i plasma at the timing of the maximum T_i (t = 4.85 s) in the LHD. The T_e and n_e data in 0.13 m < r_{eff} < 0.53 m were

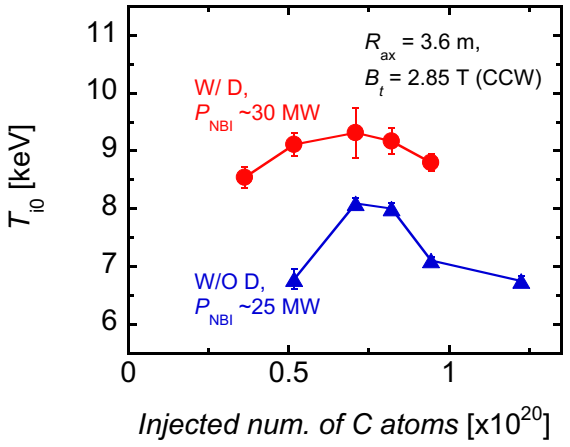

FIG. 4. The dependence of T_{i0} on the number of the carbon atoms injected using the impurity pellet injector.

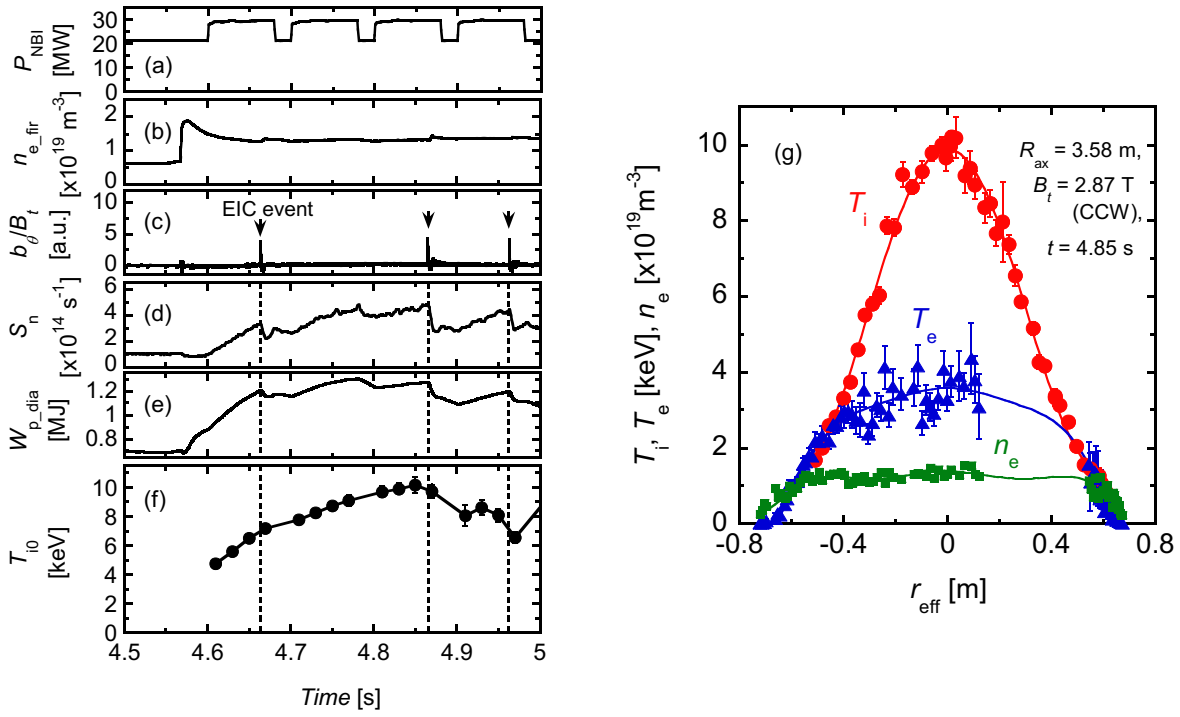

FIG. 5. The time evolution of (a) P_{NBI}, (b) n_{e_fir}, (c) b_θ/B_t, (d) the neutron emission rate S_n (e) W_{p_dia}, (f) T_{i0}, and (g) the radial profiles of T_i, T_e, and n_e of the highest-T_i plasma in the LHD.

scattered due to the stray light from the in-vessel components, thus the data are omitted in Fig.5 (g). Slightly inward-shifted configuration of R_{ax} = 3.58 m/B_t = 2.87 T (CCW) was chosen for the experiment. Also, intensive ECDC was conducted before the discharge. The plasma was sustained using high power NBI and the optimized-size carbon pellet was injected at t ~4.57 s. The central T_i was gradually increased after the additional NBI from t = 4.6 s and reached the maximum value at t = 4.85 s. The peaked T_i profile with the central value of 10 keV was successfully achieved in the discharge. The achievement of the T_i of 10 keV is a milestone toward realizing a helical reactor, which has an intrinsic advantage for steady state operation, because the T_i value is one of the important ignition conditions.

The bursty MHD event, which is a so-called energetic ion driven resistive interchange modes (EICs), was observed during the discharge. The timing of the EIC occurrence is indicated by arrows and dashed lines in Fig.5 (c)-(f). The EICs are driven by the increased pressure gradient of helically trapped energetic ions, which are mainly generated by the perpendicular NBI [59-64]. The neutron emission rate dropped associated with the EIC event. This indicates the loss of the high energy ions from the plasma. Consequently, the plasma stored energy and the ion temperature both decreased. One of the control knobs of the EICs is ECRH. The threshold of the EIC excitation increases due to the decrease of the mode width, which is proportional to $T_e^{-1/2}(\beta\,(dp_e/dr_{eff})/p_e)^{1/6}$ [61, 65, 66]. Thus the increasing T_e using ECRH is an effective technique to suppress EICs. The suppression of EICs using ECRH was reported in [61] due to the decrease of the mode width. On the other hand, degradation of the ion thermal confinement by ECRH due to the increase of T_e/T_i was also reported in several devices [67-71]. The increase in the ion thermal diffusivity χ_i with increase in the T_e/T_i during the stepwise ECRH superposition was also observed in the LHD [72]. The optimization study of ECRH for suppression of EICs with lesser degradation of ion thermal confinement will be conducted in order to realize stationary-sustained higher T_i plasmas.

4. Isotope Effect of the Confinement Characteristics of the Ion-ITB Plasmas

4.1. Realization of Higher-T_i Plasma with Deuterium

The realization of the high T_i in the deuterium experiments is not only due to the increased NBI power and the operational optimizations but also to the improvement of the ion thermal confinement of the D plasmas compared with the H plasmas. Here, the comparative results of the confinement characteristics between plasmas W/O D and W/ D are shown.

Figure 6 shows the time evolution of (a) P_{NBI}, (b) n_{e_fir}, (c) W_{p_dia}, (d) the central electron density n_{e0}, (e) the central electron temperature T_{e0}, (f) T_{i0}, and (g) the radial profiles of T_i at the timing of the maximum T_i for the typical high T_i plasmas W/O D and W/ D. The magnetic configuration was R_{ax} = 3.6 m/ B_t = 2.85 T (CCW) both for these discharges. The carbon pellet with cylindrical shape (ϕ = 1.0 mm, l = 1.0 mm) was injected at t ~4.57 s. The injected number of the carbon atom by the pellet is ~0.7×10^{20} and is optimum for obtaining high T_i plasmas as shown in Fig. 4. The increment of the electron density due to the injected carbon pellet is evaluated as ~1.4×10^{19} m^{-3}. The value is consistent with the increment of n_{e_fir} (~1.2×10^{19} m^{-3}) just after the carbon pellet injection shown in Fig. 6 (b). In ref [21], the increment of Z_{eff} was shown to be ~1 just after carbon pellet injection, decreasing to ~0.2 due to the formation of the impurity hole with the strong outward convection of the impurity [73-75].

The higher T_i plasma with higher n_e was realized for the plasma W/ D. As shown in the Fig. 6 (f), the T_i was higher in the plasma entire region for the plasma W/ D, especially the increase in the T_i around the plasma centre was emphasized due to the steepened T_i gradient in $|r_{eff}/a_{99}| < 0.25$ compared with the plasma W/O D. It was also found that the higher T_i was maintained for a longer time for the plasma W/ D. That is the T_{i0} continued to increase until 4.74 s for the plasma W/O D and 4.91 s for the plasma W/ D. On the other hand T_{e0} appeared to be slightly lower for the plasma W/ D. The energy confinement time, which was evaluated as the ratio of the total kinetic energy to the total absorbed heating power

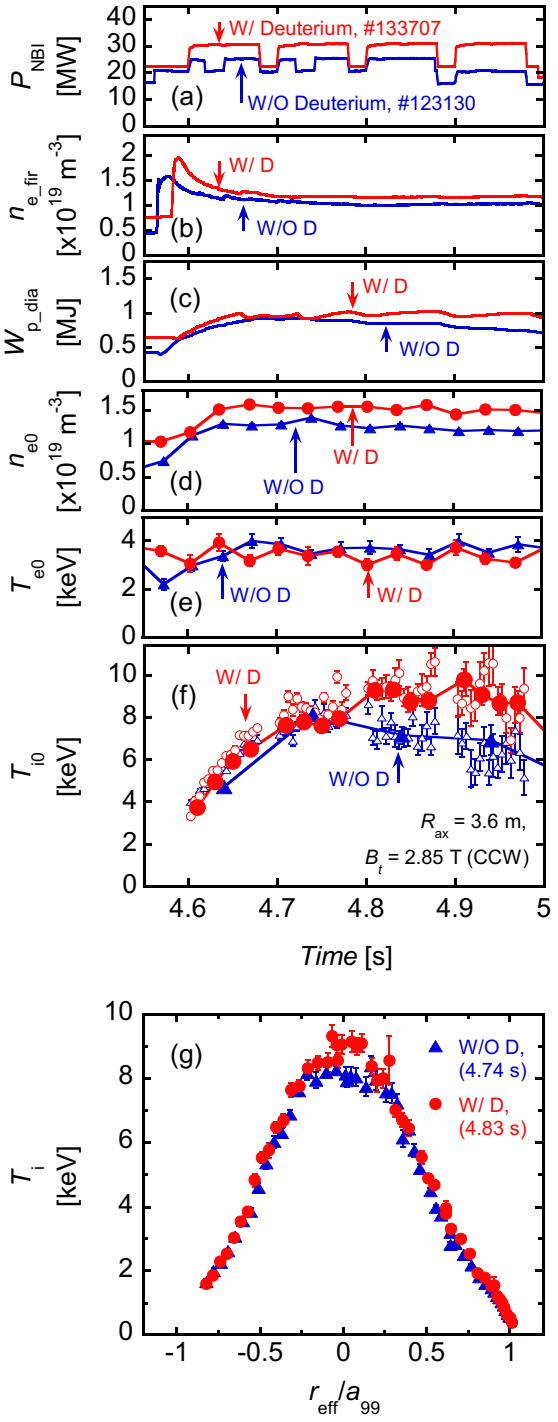

FIG. 6. The time evolution of (a) P_{NBI}, (b) n_{e_fir}, (c) W_{p_dia}, (d) n_{e0}, (e) T_{e0}, (f) T_{i0}, and (g) the radial profiles of T_i at the timing of the maximum T_i for the typical high T_i plasmas W/O D and W/ D.

from GNET [76-78] minus radiation power, was 49 ms at 4.74 s for #123130 and was 55 ms at 4.83 s for #133707. Please note that the ECRH wall conditioning with Helium gas introduced in Sec. 3.1 was conducted prior to both discharges in Fig.6. Thus a significant amount of He contaminated in the plasmas. The ratios of ion densities (n_H:n_D:n_{He}:n_C) are (0.556:0:0.407:0.037) at 4.74 s for #123130 and (0.169:0.293:0.532:0.005) at 4.83 s for #133707. The comparison of the plasma performance between H and D with higher ion purity is shown in Sec. 4.3.

4.2. Reduction of the Ion Thermal Diffusivity in the Plasma with Deuterium

Here the plasma profiles and the ion thermal confinement are compared between the plasmas W/O D and W/ D introduced in Fig. 6. Figure 7 shows the comparison of the radial profiles of (a)-(f) n_e, T_e, T_i, and the gradient, (g) T_e/T_i, and (h) the total ion heating power P_{i_tot} for the plasmas W/O D and W/ D. The ion heating power calculated using GNET was slightly lower in the W/ D case even though the total port-through NBI power was higher. In the operation W/ D, the beam energy of the perpendicular NBI was increased as mentioned in Sec. 2, leading to the enhanced deviation of the beam particles from the magnetic surfaces. This is one of the considered reasons for the decreased absorption power in the plasma W/ D. In spite of the lower heating power, higher T_i with higher n_e was realized in the plasma W/ D. The improvement of T_i and n_e were significant in the plasma central region. On the other hand T_e profiles were similar between these two plasmas and the value was slightly smaller in the central region for the plasma W/ D, leading to the lower T_e/T_i in the entire plasma region except for the plasma edge in the case W/ D.

The ion species effect on the thermal confinement in hydrogen and helium plasmas were experimentally investigated in the LHD [79]. In [79], the ion thermal diffusivity was evaluated taking account of the gyro-Bohm factor, which is defined as $A_i^{0.5}T_i^{1.5}/(aZ_i^2B_t^2)$ [9, 11-15], where A_i is the ion mass and Z_i is the nuclear charge of each ion. In the present study, the contribution of hydrogen, deuterium, helium, and carbon were taken into account for the evaluation of the effective ion thermal diffusivity. Here, we assume that the ion temperature is same among the ions and define the effective ion thermal diffusivity χ_{i_eff} normalized by the gyro-Bohm factor as

$$\text{GB normalized } \chi_{i\_eff} = \frac{1}{\frac{dT_i}{dr_{eff}} n_i T_i^{1.5}} \sum_k \frac{Q_k}{A_k^{0.5} Z_k^{-2}}, \quad (1)$$

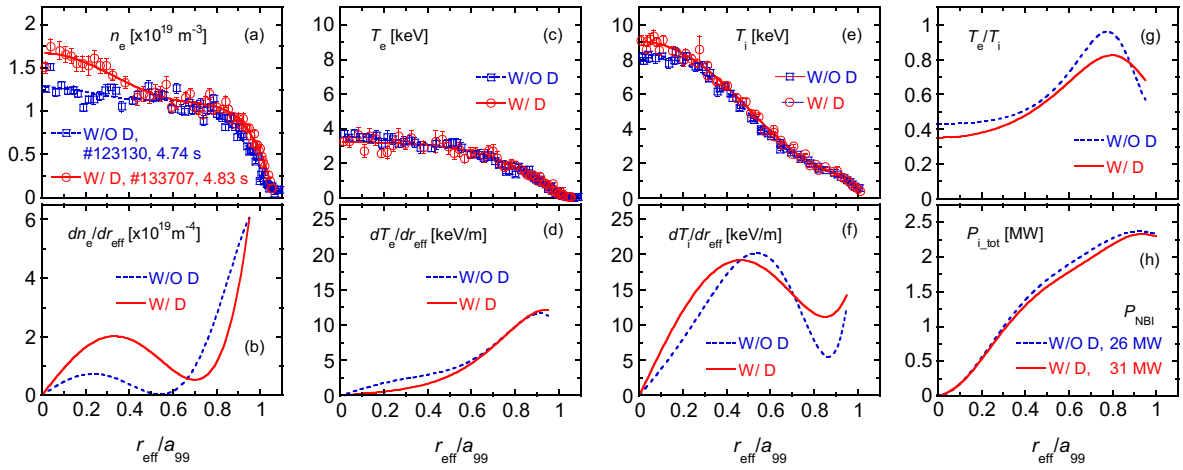

FIG. 7. The comparison of the radial profiles of (a)-(f) n_e, T_e, T_i, and the gradient, (g) T_e/T_i, and (h) the total ion heating power P_{i_tot} between the plasmas W/O D and W/ D.

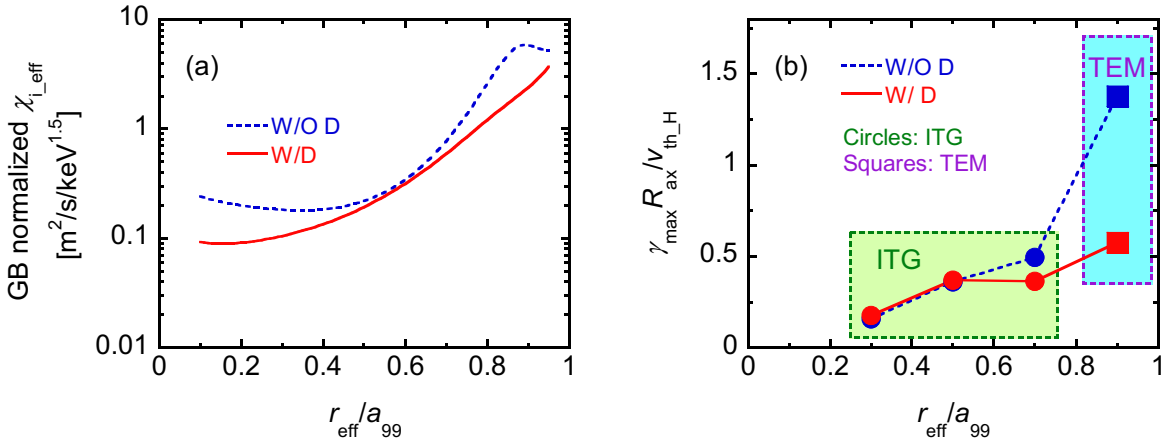

FIG. 8. The comparison of the radial profiles of (a) the effective χ_i normalized by the gyro-Bohm factor and (b) the normalized maximum linear growth rate of ITG and TEM between the plasmas W/O D and W/ D.

where Q is the heat flux and the index k represents H, D, He, and C. Figure 8 shows the comparison of the radial profiles of (a) the effective ion thermal diffusivity normalized by the gyro-Bohm factor computed using eq. (1), and (b) the maximum linear growth rate γ_{max} of ITG and TEM instability normalized by v_{th_H}/R_{ax} between the plasmas W/O D and W/ D introduced in Figs. 6 and 7, where v_{th_H} is the proton thermal speed. The Q_k was calculated using GNET and T_i was obtained from CXRS measurement. The linear growth rates of ITG/TEM were calculated using GKV taking account of the effect of the multi-ion species [12]. The effective ion thermal diffusivity was found to be smaller in the whole plasma region for the plasma W/ D. The GKV simulation showed that the dominant instability was ITG for the core region and was TEM for the plasma edge region both for the plasmas W/O D and W/ D. In the outer core region of $0.6 < r_{eff}/a_{99}$ the tendency in the radial dependence appeared to be similar between the effective ion thermal diffusivity and the linear growth rates of ITG/TEM. However, the experimentally observed difference in χ_{i_eff} for $r_{eff}/a_{99} < 0.6$ could not be explained only by the present linear simulation. Since the zonal flow generation is not taken into account in the linear simulations, non-linear calculations are required for more quantitative comparisons. Also, the stabilizing effect of the mean E_r shear, which is also not included in the present simulation model, may have impacts on the turbulent transport level. They will be addressed in future works.

4.3. Comparison of the Configuration Dependence of the Plasma Parameters between Hydrogen and Deuterium Plasmas with Higher Purity

As mentioned in Secs. 4.1 and 4.2, higher ion thermal confinement was obtained in the operation W/ D. However, those comparisons were complicated due to the contamination of the He resulting from the wall conditioning. Here, the plasma performance between H and D was compared with higher ion purity.

Figure 9 shows the n_e dependence of T_{e0} and T_{i0} in several magnetic configurations for (a), (b) H, and (c), (d) D plasmas, and the configuration dependence of (e) T_{e0}, and (f) T_{i0}. The helical coil current in these experiments was fixed as 11.4 kA (CCW) and the magnetic field strength on the axis was 2.82 T (R_{ax} = 3.64 m) ≤ B_t ≤ 2.89 T (R_{ax} = 3.55 m). The plasmas were sustained using H-NBIs with H gas puff for H plasmas and D-NBIs with D gas puff for D

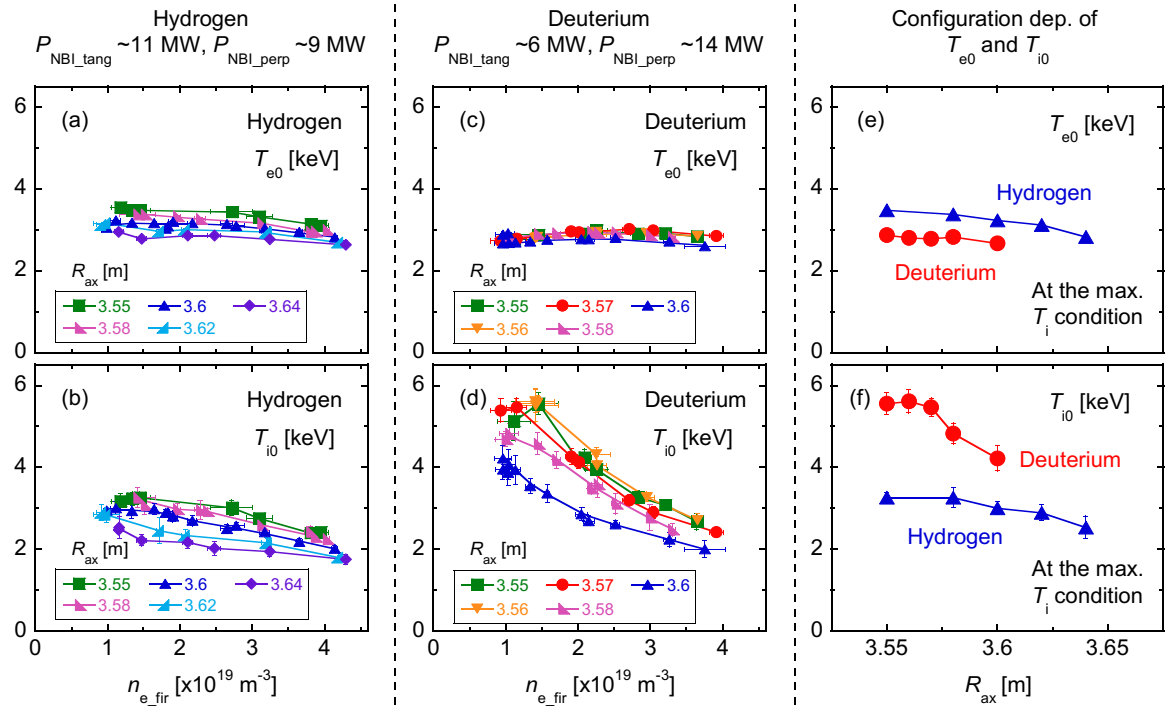

FIG. 9. The n_e dependence of T_{e0} and T_{i0} in several magnetic configurations for (a), (b) H, and (c), (d) D plasmas, and the configuration dependence of (e) T_{e0}, and (f) T_{i0}.

plasmas. The baking and the glow discharge were conducted just before the experiments. Also the ECDC operations with He were not conducted in the series of the experiment. As a result, the ratios of the ion density n_H and n_D to the total ion density were over 0.73 and 0.91, respectively, for the target discharges. The total NBI port-through power was fixed as ~20 MW for all target plasmas here. Although the total NBI power was fixed, the power allocation of the tangential beam and the perpendicular beam was different between H and D plasmas. The port-through power of the tangential NBIs and the perpendicular NBIs were ~11 MW and ~9 MW for the H operation and were ~6 MW and ~14 MW for the D operation. The T_{e0} tended to increase in the inward-shifted configuration both for the H and D plasmas. From the comparison of the configuration dependence between H and D, the T_{e0} was systematically higher in the H plasmas. In contrast to T_{e0}, the T_{i0} showed the strong dependence on the n_e and the magnetic configuration, especially in D operation. Higher T_{i0} was realized with higher n_e in the inward-shifted configuration. Also the obtained T_{i0} was found to be higher in D plasmas compared with H with the same magnetic configuration.

Clear difference in the profile of the n_e and the impurity was also found between H and D plasmas depending on the magnetic configuration. Figure 10 shows the radial profiles of $P_{i\_NBI\_abs}$, n_e, n_C, and T_i in several magnetic configurations for (a)-(d) H, and (e)-(h) D plasmas. Here $P_{i\_NBI\_abs}$ is the NBI absorption power for ion calculated using GNET. The line-averaged n_e of the data in the figures are ~1.2x10^{19} m^{-3} (± 8%) for H and ~ 1.1 x10^{19} m^{-3} (± 8%) for D. Carbon pellets were not used in the operation. Thus the carbon in the plasma was originated from the carbon divertor of the LHD. For the D plasmas, the deviation of the trapped particle orbit from the magnetic surface is larger than the H plasmas due to the larger Larmor radius, leading to the lower heating efficiency of the NBIs. Consequently the ion heating power was similar between H and D with the same configuration of R_{ax} = 3.55 m and the 3.6 m even though the port through power of the perpendicular NBIs, which mainly

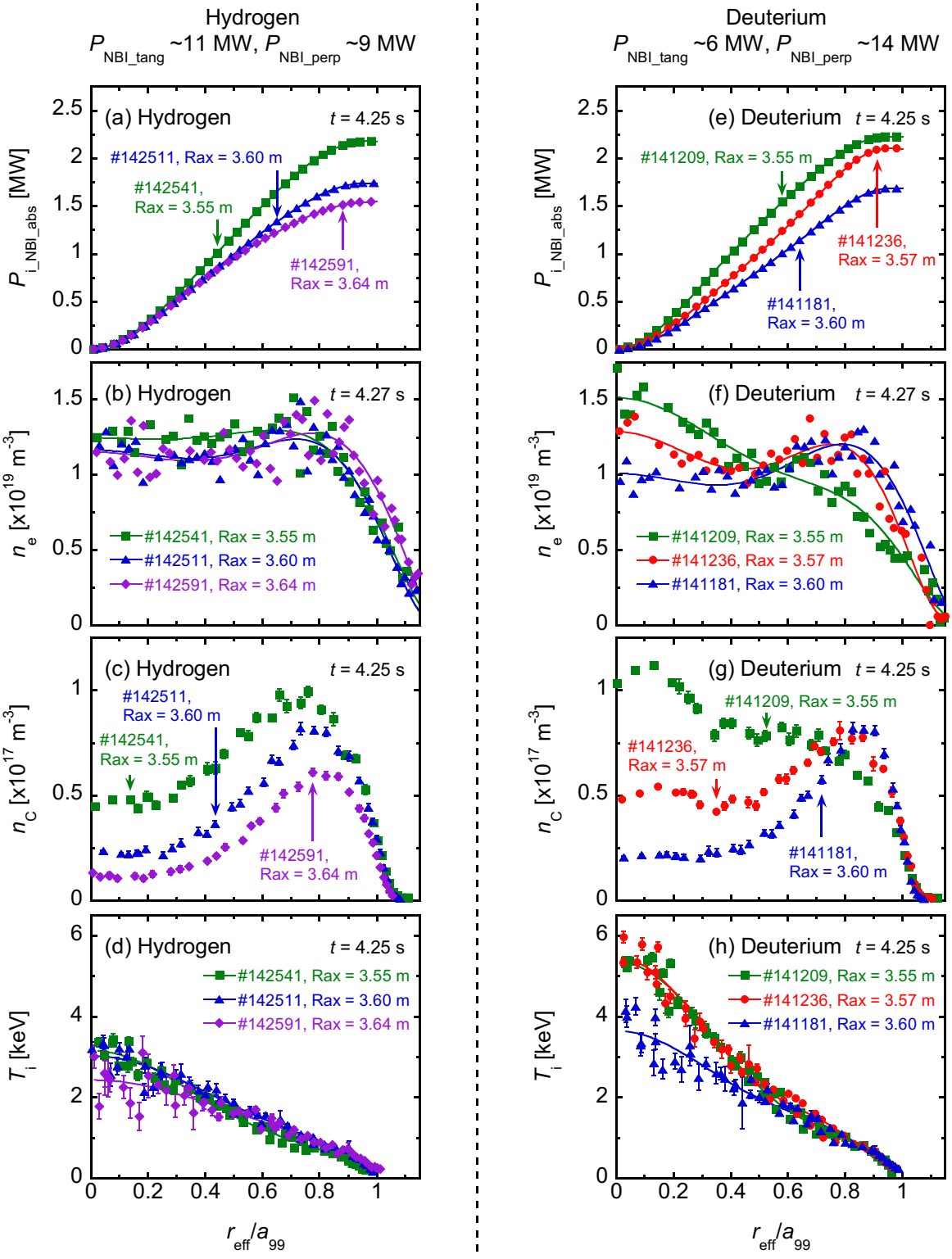

FIG. 10. The radial profiles of $P_{i\_NBI\_abs}$, n_e, n_C, and T_i in several magnetic configurations for (a)-(d) H, and (e)-(h) D plasmas.

contribute to ion heating, was dominant for the D plasmas. The NBI heating power for ion also tended to increase in the inward shifted configuration. This is due to the decrease of the orbit loss of the NBI ions in the inward shifted configuration [77]. The flat or slightly hollow profile of the n_e and the hollow profile of the n_C so-called impurity hole was formed for H plasmas. The hollowness of the n_C profile became stronger in the outward-shifted

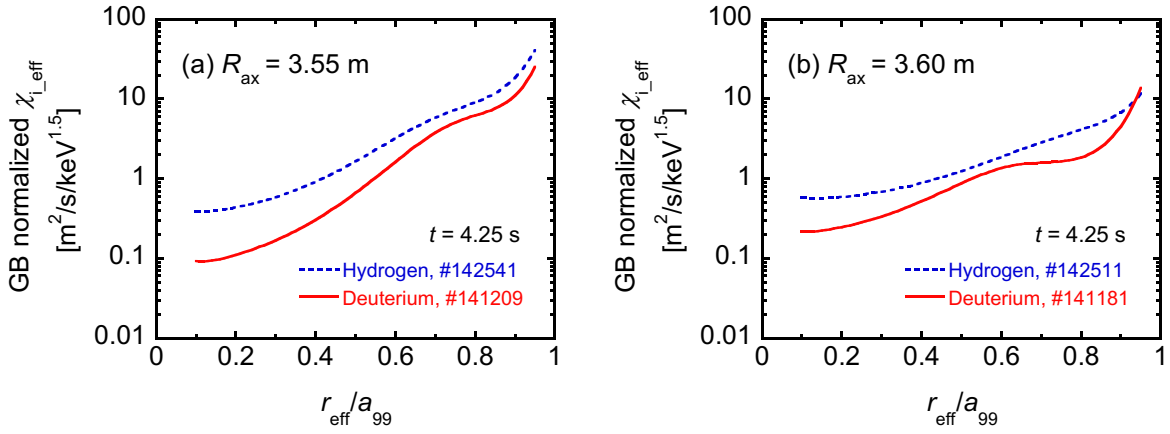

FIG. 11. The comparison of the radial profiles of the effective χ_i normalized by the gyro-Bohm factor between the H and D plasmas for the magnetic configurations (a) R_{ax} = 3.55 m and (b) R_{ax} = 3.6 m.

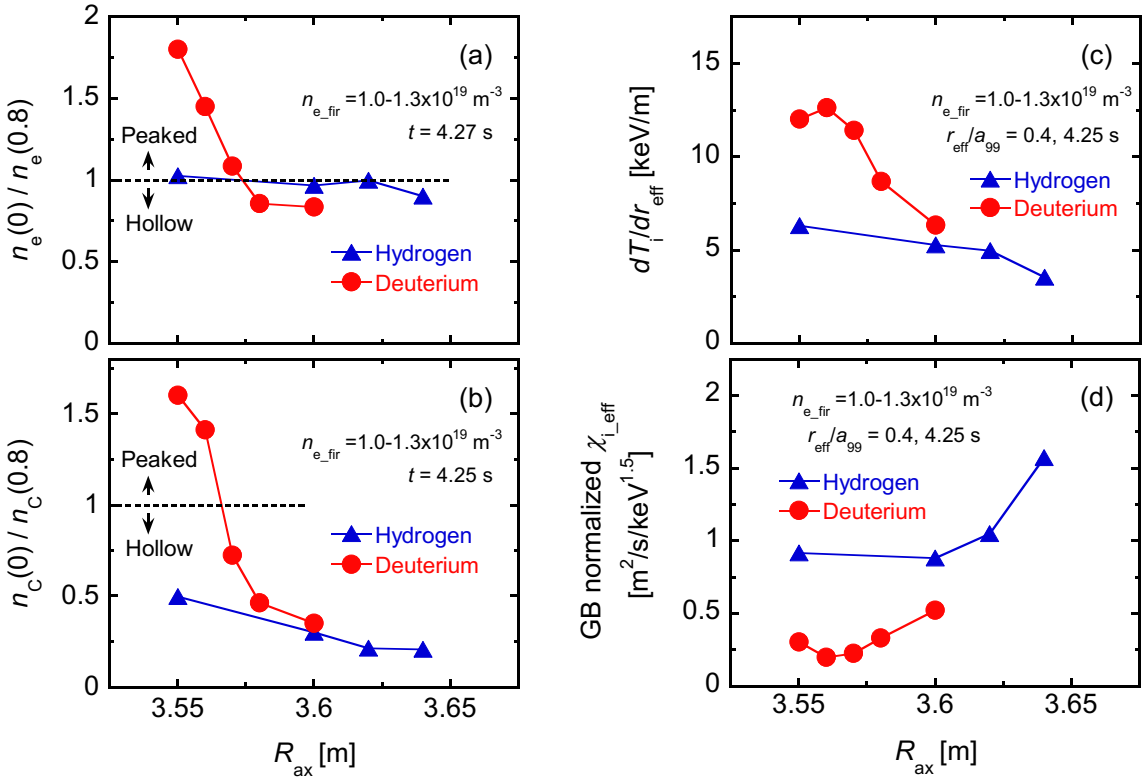

FIG. 12. The configuration dependence of (a) the peaking factor of the n_e profile, (b) the peaking factor of the n_C profile, (c) dT_i/dr_{eff}, and (d) the effective χ_i normalized by the gyro-Bohm factor at the r_{eff}/a_{99} = 0.4. The triangles and the circles are the data for hydrogen and deuterium, respectively.

configuration and was consistent with the previous experimental results [74]. On the other hand, the shape of the n_e and the n_C profiles of the D plasmas were found to depend on the magnetic configuration. Although the profiles of the n_e and the n_C of the D plasma were hollow for the R_{ax} = 3.6 m case as with H case, those were peaked for the inward-shifted configuration of R_{ax} = 3.55 m and were qualitatively different with the H case of R_{ax} = 3.55 m. The intrinsic formation of the peaked n_C profile has never observed in the i-ITB plasmas in the LHD using hydrogen. The central T_i and the T_i gradient in the core region were larger in the inward-shifted configuration of R_{ax} = 3.55 m compared with those of R_{ax} = 3.6 m.

Interestingly, high T_i, hollow n_C, and peaked n_e were simultaneously realized in the case of R_{ax} = 3.57 m for the D operation although the bump was formed in the n_e profile around r_{eff}/a_{99} = 0.8.

Figure 11 shows the comparison of the radial profiles of the effective χ_i normalized by the gyro-Bohm factor between the H and D plasmas for the magnetic configurations (a) R_{ax} = 3.55 m and (b) R_{ax} = 3.6 m. The effective χ_i clearly reduced for the D plasmas in the plasma entire region both for the configurations of R_{ax} = 3.55 m and 3.6 m. Especially the improvement of the ion thermal confinement in D plasma was significant in the inner half of the minor radius for the configuration of R_{ax} = 3.55 m.

The configuration dependence of the profile shape of n_e, n_C, and the ion thermal confinement is summarized in Fig. 12. Figure 12 shows the configuration dependence of (a) the peaking factor of the n_e profile, (b) the peaking factor of the n_C profile, (c) the ion temperature gradient, and (d) the effective χ_i normalized by the gyro-Bohm factor at the r_{eff}/a_{99} = 0.4. The triangles and the circles are the data for H and D, respectively. Here the peaking factor of the radial profiles of n_e and n_C are defined as the ratio of the value at r_{eff}/a_{99} = 0 to the value at r_{eff}/a_{99} = 0.8. The line-averaged n_e of the data in the figures are 1.0-1.3x10^{19} m^{-3}. From the configuration dependence of the n_e peaking factor and the n_C peaking factor in the H operation, the n_e profiles were almost flat or slightly hollow shape and the hollowness in the n_C profile became stronger in the outward-shifted configuration as mentioned above. The T_i gradient became larger in the inward-shifted configuration. In the D operation, the peaking factor of the n_e and the n_C, and the T_i gradient were significantly increased in the inward-shifted configuration. These tendencies were qualitatively different from those of the H plasmas. The peaked n_C profile was also found in the high T_i plasmas W/ D using a carbon pellet [80]. As can be seen in Fig. 12 (d), the effective χ_i was found to be systematically smaller in the D operations than those in the H operations.

5. Characteristics of the Electron-ITB Formation and the Isotope Effect

5.1. Effect of the Current Drive Direction on the T_e Profile

In the previous sections, the difference in the ion thermal confinement of the ion-ITB plasmas between H and D was discussed. We also conducted the high T_e experiment using high power ECRH with H and D. Here the confinement characteristics of the high T_e plasmas associated with an e-ITB are compared between H and D.

Before the comparison of the thermal confinement of the e-ITB plasmas between H and D, the performance of the ECRH plasma depending on the ECRH injection direction is introduced. Figure 13 shows the time evolution of (a) the ECRH injection power P_{ECRH} and P_{NBI}, (b) n_{e_fir}, (c) the plasma current I_p, and (d) T_{e0} and the radial profiles of (e) T_e and (f) n_e at 4.37 s for three different EC injection conditions. Those plasmas were produced using co ECCD (Co-ECCD), balanced injected ECRH, and counter ECCD (Ctr-ECCD), with the same P_{ECRH} of 3.4 MW. The magnetic configuration was R_{ax} = 3.6 m/ B_t = 2.705 T and the direction of the toroidal magnetic field was clockwise (CW). Here "Co-ECCD" means the ECCD injection to increase the rotational transform ι and "Ctr-ECCD" means to decrease ι. The relation among the direction of B_t, the EC beam, and the driven current is summarized in Tab. I. The line-averaged-electron density was almost the same value of ~2x10^{19} m^{-3} among the three discharges. Although the NBI was superposed on the ECRH plasmas from 3.5 s, this is the perpendicular injection thus the beam had no contribution as NBCD. Unfortunately the ι profiles were not measured in the three cases but the ι is considered to change as intended from the change in the I_p. As can be seen in Fig.13 (e), the T_e profile was clearly affected by

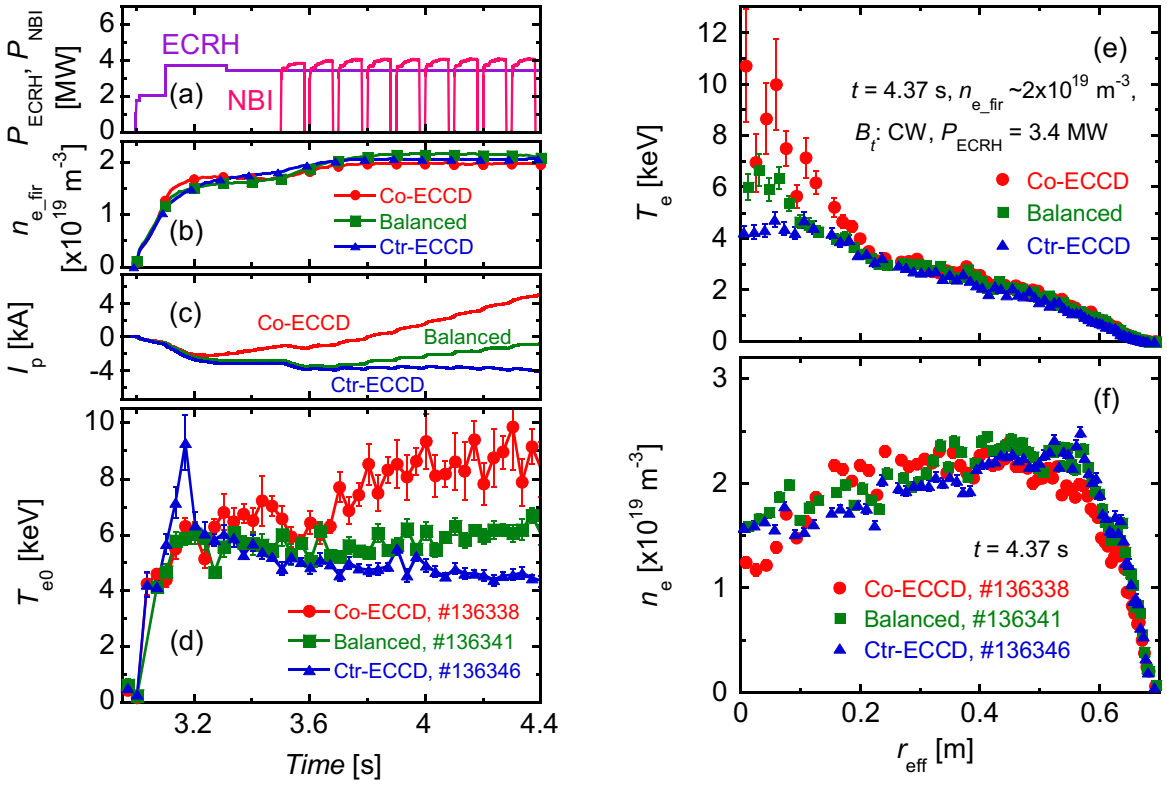

FIG. 13. The time evolution of (a) P_{ECRH} and P_{NBI}, (b) n_{e_fir}, (c) I_p, and (d) T_{e0} and the radial profiles of (e) T_e and (f) n_e at 4.37 s for three different EC injection conditions with the toroidal magnetic field direction of CW.

the direction of the ECRH injection direction. Centre-peaked T_e profile and high T_{e0} were obtained for the Co-ECCD case. On the other hand, the T_e profile was broad for the Ctr-ECCD case. For the balanced injection case, the T_{e0} was between the value of Co-ECCD and Ctr-ECCD.

TABLE I. The relation among the direction of B_t, the EC beam, and the driven current.

B_t direction	EC beam direction	Driven current direction
CW	CW	CCW (Ctr)
	CCW	CW (Co)
CCW	CW	CCW (Co)
	CCW	CW (Ctr)

This T_e profile change with the ECCD direction was found not to depend on the polarity of the confinement magnetic field. Figure 14 shows the comparison of the profiles between Co-ECCD and Ctr-ECCD for (a) T_e and (b) $\iota/2\pi$ under the magnetic configuration of R_{ax} = 3.6 m/ B_t = 2.705 T with the toroidal field direction of CCW, which was opposite magnetic polarity to the operation of Fig. 13. The ECRH power and the line-averaged-electron density were 2.8 MW and ~2x10^{19} m^{-3}, respectively. The T_e profile was also changed with the ECCD direction and the dependence was the same as that shown in Fig. 13. That is, the centre-peaked T_e was realized for the Co-ECCD case. The ι profile was changed in the plasma central region depending on the ECCD direction. In the previous study, core temperature degradation was observed due to the stochastization of the confinement magnetic field [81, 82]. In those papers, the stochastization in the plasma core region was concluded to be originated from the weakened $d\iota/dr$ at the low order rational surface of $\iota/2\pi$ = 0.5 and the flattened temperature profile was appeared in the inner area from the position of $\iota/2\pi$ = 0.5. In the present research, higher T_e was observed in the low ι shear case with Co-

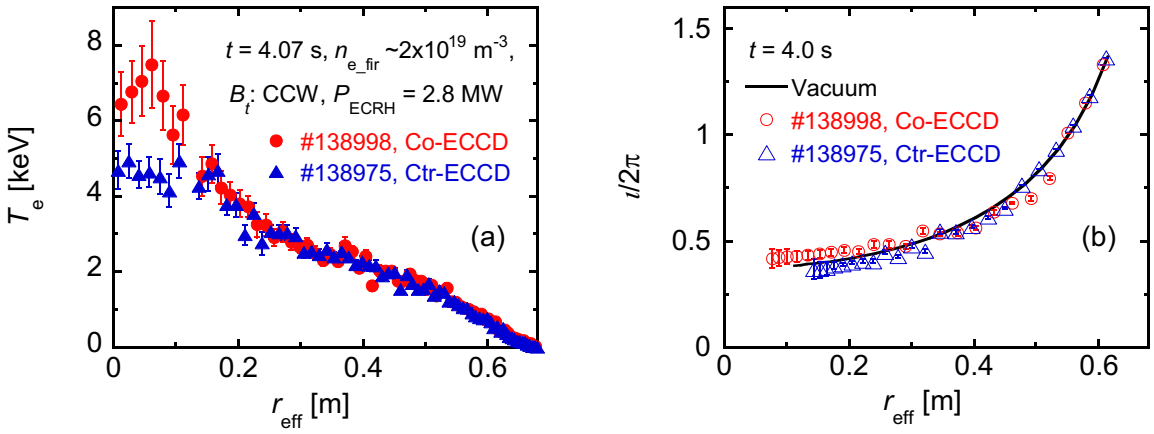

FIG. 14. Comparison of the radial profiles of (a) T_e and (b) $\iota/2\pi$ between Co-ECCD and Ctr-ECCD with the toroidal magnetic field direction of CCW.

ECCD and the bifurcation point of the T_e profile was r_{eff} ~0.15 m, which is different from the $\iota/2\pi$ = 0.5 position of r_{eff} ~0.3 m. Thus, the degradation of the core T_e in the Ctr-ECCD observed in the experiment is considered to be a different phenomenon from the stochastization of the magnetic field due to the weakened $d\iota/dr$ at the position of $\iota/2\pi$ = 0.5. We will continue the investigation for clarifying the mechanism of the T_e profile formation depending on the ECCD direction in order to establish the temperature profile control for the maximization and/or the optimization of the plasma performance.

5.2. Reduction in the Electron Thermal Diffusivity of e-ITB Plasmas in the Deuterium Operation

As introduced in the previous section, higher T_e with the strong e-ITB was realized using Co-ECCD in the LHD although the mechanism has not been clarified. In order to investigate the isotope effect on the thermal confinement of the e-ITB plasmas, the target plasmas for the comparison were chosen from the Co-ECCD condition. Figure 15 shows the radial profiles of (a) the absorbed ECRH power density p_{ECRH} and the volume integral P_{ECRH}, (b) n_e, (c) T_e, (d) the electron pressure n_eT_e, and (e) the electron thermal diffusivity χ_e for H and D with approximately the same n_{e_fir} ~2.4x10^{19} m^{-3}. The magnetic configuration was R_{ax} = 3.6 m/ B_t = 2.705 T (CW) both for the H and D plasmas. The purity of the target ions are $n_H/(n_H+n_D+n_{He})$ = 0.94 for the H plasma and $n_D/(n_H+n_D+n_{He})$ = 0.81 for the D plasma. Unfortunately, one gyrotron had trouble in the D experimental phase and the gyrotron could not be operated in the experiments. Thus the total ECRH injection power became smaller in the D experiments. In spite of the decreased ECRH power for the D plasma, almost the same profiles of T_e and n_eT_e with H plasma were realized. Although the n_{e_fir} was fixed as ~2.4x10^{19} m^{-3}, the n_e profile was slightly different between H and D plasma. The χ_e was evaluated from the power balance analysis and was decreased in $r_{eff}/a_{99} < 0.45$ both for the H and the D plasma due to the formation of the e-ITB. From the comparison between these two discharges, χ_e was clearly reduced in D plasma except for the plasma edge. The systematic data for the comparison of the global energy confinement of the e-ITB plasmas between H and D were also obtained with the n_{e_fir} of 1.5-4.7x10^{19} m^{-3} and the injection ECRH power of 1-3 MW. The energy confinement in D plasmas was found to be statistically 10-20% higher than H plasmas [83].

The linear-microinstability simulation using GKV was also applied for the high T_e plasmas. Figure 16 shows the dependence of the linear growth rate of ITG and TEM on $k_y\rho_t$ at three different positions around the foot point of e-ITB for (a) H and (b) D, where k_y is the wave

number of the eigenmode perpendicular to the magnetic field line and ρ_t is the ion thermal gyroradius. The same normalization with v_{th_H} was imposed to the linear growth rates both for the H and the D cases for the direct comparison of the absolute value. The GKV simulation showed the mixture of TEM and ITG depending on the radius. The linear growth rate of TEM/ITG significantly reduced in the D plasma. Note that both the slight difference of T_i gradient and the large difference of n_e gradient lead significantly different radial dependence of the linear growth rate, even though the T_e profiles are similar in the H and D plasmas. The normalized gradient T_e, T_i, and n_e at r_{eff}/a_{99} = 0.6 are R_{ax}/L_{Te} = 8.87 for H and 8.81 for D, R_{ax}/L_{Ti} = 4.64 for H and 6.80 for D, and R_{ax}/L_{ne} = -7.34 for H and 0.124 for D. For further quantitative study, the non-linear simulation taking account of the effect of the mean E_r shear is required and will be carried out as future works.

6. Summary

The deuterium operation was initiated in the LHD in 2017. In the first campaign of the deuterium experiments, we successfully extended the high temperature regime in the LHD. The new record of the ion temperature of 10 keV associated with the ion internal transport barrier (ITB) was achieved due to the upgraded NBI, several operational optimizations such as the wall conditioning, the quantity of the impurity, and the magnetic configuration. In order to achieve higher T_i and to sustain high T_i plasma, the EIC event must be suppressed. The confinement improvement with D also contributed to the increase in the T_i. From the systematic comparison of the transport analyses between the high-purity H and D plasmas with the several magnetic configurations, the effective χ_i was found to be smaller in the D plasmas. The impurity behaviour of the i-ITB plasmas was found to be different between H and D. The shape of the n_C profile depends on the magnetic configuration for D plasmas. The n_C profile became peaked intrinsically in the inward-shifted configuration and was different from the hollow n_C profile so-called "impurity hole," which has been usually observed in the i-ITB plasmas in the LHD using hydrogen. With regard to the e-ITB plasmas, almost the same profiles of the electron temperature and the electron pressure between H and D plasma were confirmed in spite of the decreased ECRH power for the D plasma, this was due to the reduction in the χ_e in D plasmas. The GKV simulation showed the linear growth rate of TEM/ITG significantly reduced in the D plasma with e-ITB. For the i-ITB plasmas, the

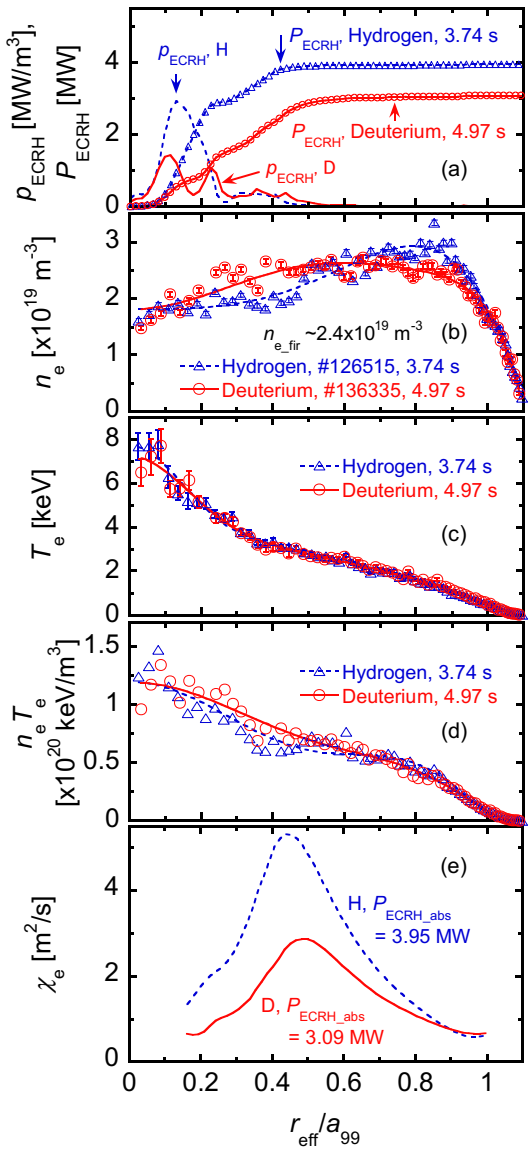

FIG. 15. The radial profiles of (a) p_{ECRH} and P_{ECRH}, (b) n_e, (c) T_e, (d) n_eT_e, and (e) χ_e for H and D with approximately the same n_{e_fir} and the different ECH power.

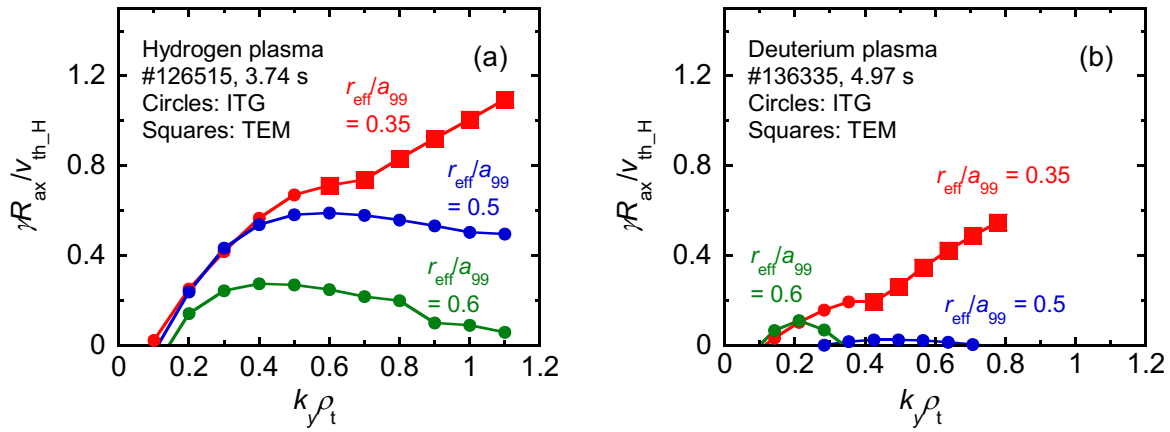

FIG. 16. The linear growth rate of ITG and TEM in the e-ITB plasmas for (a) hydrogen, and (b) deuterium.

improvement of the core ion thermal confinement in the plasma with D still has not yet been explained by the linear simulation of the GKV. For further quantitative study, the non-linear simulation taking account of the effect of the mean E_r is required. Also, the results from the first campaign of the LHD deuterium experiment presented in the paper represent the first analyses. More detailed studies will be conducted in the near future.

Acknowledgments

This work was supported by NIFS grants ULRR701, 702, 801, 808, 809, KLPR036.

References

[1] SCHISSEL D.P. et al., Nucl. Fusion **29** (1989) 185.

[2] BESSENRODT-WEBERPALS M. et al., Nucl. Fusion **33** (1993) 1205.

[3] STROTH U. et al., Phys. Scr. **51** (1995) 655.

[4] CORDEY J.G. et al., Nucl. Fusion **39** (1999) 301.

[5] URANO H. et al., Phys. Rev. Lett. **109** (2012) 125001.

[6] MAGGI C.F. et al., Plasma Phys. Control. Fusion **60** (2018) 014045.

[7] TOKAR M.Z., KALUPIN D. and UNTERBERG B., Phys. Rev. Lett. **92** (2004) 215001.

[8] SUGAMA H. and WATANABE T.-H., Phys. Plasmas **16** (2009) 056101.

[9] PUSZTAI I., CANDY J. and GOHIL P., Phys. Plasmas **18** (2011) 122501.

[10] WATANABE T.-H., SUGAMA H. and NUNAMI M., Nucl. Fusion **51** (2011) 123003.

[11] BUSTOS A. et al., Phys. Plasmas **22** (2015) 012305.

[12] NAKATA M. et al., Comput. Phys. Commun. **197** (2015) 61.

[13] NAKATA M. et al., Plasma Phys. Control. Fusion **58** (2016) 074008.

[14] NUNAMI M. et al., Plasma Phys. Control. Fusion **59** (2017) 044013.

[15] NAKATA M. et al., Phys. Rev. Lett. **118** (2017) 165002.

[16] WAGNER F. et al., Phys. Rev. Lett. **49** (1982) 1408.

[17] KOIDE Y. et al., Phys. Rev. Lett. **49** (1994) 3662.

[18] FUJISAWA A., Plasma Phys. Control. Fusion **45** (2003) R1.

[19] FUJITA T. et al., Plasma Phys. Control. Fusion **46** (2004) A35.

[20] KANEKO O. et al., Plasma Fusion Research **4** (2009) 027.

[21] IDA K. et al., Nucl. Fusion **49** (2009) 095024.

[22] IDA K. et al., Nucl. Fusion **50** (2010) 064007.

[23] NAGAOKA K. et al., Nucl. Fusion **51** (2011) 083022.

[24] TAKAHASHI H. et al., Nucl. Fusion **53** (2013) 073034.

[25] SAKAMOTO Y. et al., Nucl. Fusion **41** (2001) 865.

[26] IDA K. et al., Phys. Rev. Lett. **91** (2003) 085003.

[27] TAKEIRI Y. et al., Fusion Sci. Technol. **46** (2004) 106.

[28] SHIMOZUMA T. et al., Nucl. Fusion **45** (2005) 1396.

[29] TAKAHASHI H. et al., Phys. Plasmas **21** (2014) 061506.

[30] YOSHINUMA M. et al., Fusion Sci. Technol. **58** (2010) 375.

[31] IDO T. et al., Rev. Sci. Instrm. **77** (2006) 10F523.

[32] YOKOYAMA M. et al., Nucl. Fusion **47** (2007) 1213.

[33] KLINGER T. et al., Plasma Phys. Control. Fusion **59** (2017) 014018.

[34] OSAKABE M. et al., Fusion Sci. Technol. **72** (2017) 199.

[35] TAKEIRI Y., IEEE Trans. Plasma Sci. (2017) 1. https://ieeexplore.ieee.org/document/8122295/

[36] IIYOSHI A et al., Nucl. Fusion **39** (1999) 1245.

[37] YAMADA Y. for the LHD Experiment Group, Nucl. Fusion **51** (2011) 094021.

[38] KANEKO O. et al., Nucl. Fusion **53** (2013) 104015.

[39] IDA K. et al., Nucl. Fusion **55** (2015) 104018.

[40] TAKEIRI Y. et al., Nucl. Fusion **57** (2017) 102023.

[41] TAKEIRI Y. et al., Fusion Sci. Technol. **58** (2010) 482.

[42] OSAKABE M. et al., 2007 Proc. 17th Int. Toki Conf./16th Int. Stellarator/Heliotron Workshop 2007 (Toki, Japan) P2-079 http://www.nifs.ac.jp/itc/itc17/file/PDF proceedings/poster2/P2-079.pdf.

[43] SHIMOZUMA T. et al., Fusion Sci. Technol. **58**, (2010) 530.

[44] TAKAHASHI H. et al., Fusion Sci. Technol. **57** (2010) 19.

[45] TAKAHASHI H. et al., Plasma Fusion Research **9** (2014) 1402050.

[46] TAKAHASHI H. et al., J. Nucl. Mater. **463** (2015) 1100.

[47] YAMADA H. et al., Plasma Phys. Control. Fusion **43** (2001) A55.

[48] MURAKAMI S. Nucl. Fusion **42** (2002) L19.

[49] YAMADA Y. et al., Nucl. Fusion **45** (2005) 1684.

[50] TANAKA K. et al., Nucl. Fusion **46** (2006) 110.
[51] TANAKA K. et al., Fusion Sci. Technol. **51** (2007) 97.
[52] FUNABA H. et al., Plasma Fusion Research **3** (2008) 022.
[53] MIYAZAWA J. et al., Fusion Sci. Technol. **58** (2010) 29.
[54] DONG J.Q. et al., Phys. Plasmas **1** (1994) 3635.
[55] DONG J.Q. and HORTON W., Phys. Plasmas **2** (1995) 3412.
[56] FU X.Y. et al., Phys. Plasmas **4** (1997) 588.
[57] MORITA S. et al., Plasma Sci. Technol. **13** (2011) 290.
[58] OSAKABE M. et al., Plasma Phys. Control. Fusion **56** (2014) 095011.
[59] DU X.D. et al., Phys. Rev. Lett. **114** (2015) 155003.
[60] DU X.D. et al., Nucl. Fusion **56** (2016) 016002.
[61] DU X.D. et al., Phys. Rev. Lett. **118** (2017) 125001.
[62] OGAWA K. et al., Nucl. Fusion **58** (2018) 044001.
[63] MICHAEL C.A. et al., Nucl. Fusion **58** (2018) 046013.
[64] BANDO T. et al., Nucl. Fusion **58** (2018) 082025.
[65] BIGLARI H. and CHEN L., Phys. Fluids **29** (1986) 2960.
[66] CARREAS B.A. and DIAMOND P.H., Phys. Fluids B **1** (1989) 1011.
[67] SCHMITZ L. et al., Nucl. Fusion **52** (2012) 023003.
[68] SOMMER F. et al., Nucl. Fusion **55** (2015) 033006.
[69] YOSHIDA M. et al., Nucl. Fusion **55** (2015) 073014.
[70] NAGAOKA K. et al., Nucl. Fusion **55** (2015) 113020.
[71] YU D.L. et al., Nucl. Fusion **56** (2016) 056003.
[72] TAKAHASHI H. et al., Nucl. Fusion **57** (2017) 086029.
[73] YOSHINUMA M. et al., Nucl. Fusion **49** (2009) 062002.
[74] IDA K. et al., Phys. Plasma **16** (2009) 056111.
[75] YOSHINUMA M. et al., Nucl. Fusion **55** (2015) 083017.
[76] MURAKAMI S. et al., Nucl. Fusion **40** (2000) 693.
[77] MURAKAMI S. et al., Fusion Sci. Technol. **46** (2004) 241.
[78] YAMAGUCHI H. and MURAKAMI S., Nucl. Fusion **56** (2016) 026003.
[79] TANAKA K. et al., Nucl. Fusion **57** (2017) 116005.
[80] MUKAI K. et al., Plasma Phys. Control. Fusion in press.
[81] IDA K. et al., New J. Phys. **15** (2013) 013061.
[82] IDA K. et al., Nat. Commun. **6** (2015) 5816.
[83] WARMER F. et al., to be published in Nucl. Fusion.